PHYSICS

Longitudinal and transverse electron paramagnetic resonance in a scanning tunneling microscope

Tom S. Seifert[1]*, Stepan Kovarik[1], Dominik M. Juraschek[1,2], Nicola A. Spaldin[1], Pietro Gambardella[1], Sebastian Stepanow[1]*

Electron paramagnetic resonance (EPR) spectroscopy is widely used to characterize paramagnetic complexes. Recently, EPR combined with scanning tunneling microscopy (STM) achieved single-spin sensitivity with sub-angstrom spatial resolution. The excitation mechanism of EPR in STM, however, is broadly debated, raising concerns about widespread application of this technique. We present an extensive experimental study and modeling of EPR-STM of Fe and hydrogenated Ti atoms on a MgO surface. Our results support a piezoelectric coupling mechanism, in which the EPR species oscillate adiabatically in the inhomogeneous magnetic field of the STM tip. An analysis based on Bloch equations combined with atomic-multiplet calculations identifies different EPR driving forces. Specifically, transverse magnetic field gradients drive the spin-1/2 hydrogenated Ti, whereas longitudinal magnetic field gradients drive the spin-2 Fe. Also, our results highlight the potential of piezoelectric coupling to induce electric dipole moments, thereby broadening the scope of EPR-STM to nonpolar species and nonlinear excitation schemes.

INTRODUCTION

Combining the nanometer spatial resolution of a scanning tunneling microscope (STM) with the outstanding energy resolution of electron paramagnetic resonance (EPR) allows for the study of magnetic properties and interactions at the atomic scale with sensitivity to excitations surpassing the thermal resolution limit of STM by orders of magnitude (*1*). EPR-STM has been successfully used to study transition metal atoms adsorbed on MgO and their interactions (*1*–*3*) using a resonant continuous-wave radio frequency (rf) excitation (*4*–*11*). Moreover, pulsed rf schemes have been used to coherently drive EPR excitations in single atoms (*12*). These developments open the way for further applications of EPR-STM, including the storage and retrieval of quantum information from surface spins (*13*), measurements of the relaxation time of single-molecule magnets (*14*, *15*), and the characterization of active sites and intermediate reaction species in catalysis (*16*, *17*).

Despite early EPR-STM proposals using nonmagnetic tips (*18*, *19*) and recent experimental achievements using spin-polarized tips (*1*–*12*), the driving mechanism of EPR-STM remains under debate. The central idea of EPR is that rf photons excite unpaired electrons to a higher energy spin state, which can be probed experimentally. The mechanisms underpinning the excitation and detection of EPR within an STM junction under simultaneous dc and rf bias, however, are not directly evident, particularly because the direct excitation of the EPR species by the magnetic field components of the rf tunneling and displacement currents are estimated to be negligible (*7*, *10*). In addition, the scattering of tunneling electrons at the spin center is relatively strong, thus disturbing the free evolution of the magnetic states. Reproducible EPR-STM experiments require the use of a magnetic tip (*1*–*12*), which further complicates the modeling of the STM junction. Several EPR-STM excitation and detection mechanisms have been proposed (*19*–*26*), including modulation of the tunneling barrier by the rf electric field (*23*), breathing of the density of states mediated by spin-orbit coupling (*19*), spin torque due to tunneling electrons (*24*), and piezoelectric coupling (PEC) of the rf electric field to the magnetic adatom (*22*). In the PEC mechanism, the oscillating electric field couples to the electric dipole of the EPR species and induces vibrations in the inhomogeneous magnetic field of the nearby magnetic STM tip leading to an effective oscillating magnetic field that drives the EPR transitions. In the original work in (*1*), the electric field–induced motion of the atoms was already proposed; however, the EPR transitions were ascribed to modulations of the crystal field operators. Supporting experimental data for each of these mechanisms are limited. Yang *et al.* (*7*) analyzed EPR-STM spectra of hydrogenated Ti (TiH) based on the PEC model and found a disagreement by a factor of 40 with the rf atomic displacement calculated by theory within the harmonic approximation of the local bond vibrations. In addition, Willke *et al.* (*8*) concluded that the EPR-STM driving force for TiH is proportional to the tunneling current, which is consistent with the PEC model (*4*, *22*), but the limited experimental data did not allow for a conclusive proof and discrimination from other models. It is still an open question which selection rules apply for the EPR-STM transitions, e.g., between the high spin and orbital moment ground-state doublet of Fe on MgO/Ag(100) as compared to conventional EPR where only magnetic dipole allowed transitions are accessible (*1*). These shortcomings, as well as the importance of designing future EPR-STM investigations based on the correct model, call for a comprehensive experimental and modeling approach to exploring the full parameter space of EPR-STM to reveal the driving mechanism.

In this work, we present a combined experimental and theoretical EPR-STM investigation of single Fe and TiH adatoms adsorbed on two monolayers of MgO/Ag(100). To limit the number of free parameters, we perform the measurements using the same magnetic tip and use a broad range of excitation conditions, which allows us to identify the dominant EPR excitation sources. An extended discussion of the role of the magnetic tip is reported in section S1. We choose Fe and Ti because they have been characterized previously by EPR-STM (*1*, *2*, *10*). Fe atoms on MgO/Ag(100) were also studied by x-ray magnetic circular dichroism, inelastic tunneling spectroscopy,

[1]Department of Materials, ETH Zürich, 8093 Zürich, Switzerland. [2]Harvard John A. Paulson School of Engineering and Applied Sciences, Harvard University, Cambridge, MA 02138, USA.
*Corresponding author. Email: tom.seifert@mat.ethz.ch (T.S.S.); sebastian.stepanow@mat.ethz.ch (S.S.)

and ligand field theory, which provide a consistent description of the Fe wave functions within an atomic-multiplet model (*27*). In contrast to most previous EPR-STM works, we use an external magnetic field that is strictly out of plane. To assess our data against different EPR-STM mechanisms, we completely characterize the vector magnetic field of the STM tip, including exchange and dipolar contributions and extract the Rabi frequency Ω from the EPR spectra, thus inferring the EPR driving force for our broad range of experimental conditions. This includes an extensive analysis of the dependence of the EPR signal on the external magnetic field B_{ext}, the rf voltage amplitude V_{rf}, the dc voltage V_{dc}, and the dc set point current I_{dc}. Thereby, we acquired more than 100 spectra within the EPR-STM parameter space using the same magnetic microtip at different standoff distances (s) from the surface, where s is the distance from point contact between the adatom and the STM tip. A qualitative assessment of different EPR-STM mechanisms shows that the Rabi frequency is consistent with a PEC model. To provide a more stringent quantitative comparison between theory and experiment, we evaluate the Rabi rate predicted by the PEC model by computing the rf electric field–induced displacement of the EPR species from first principles without relying on the harmonic approximation of the phonon dispersion curves and determining the relevant EPR transition matrix elements by multiplet calculations. We find quantitative agreement with our entire dataset. Our theoretical treatment reveals that state mixing enables EPR transitions between magnetic dipole–forbidden states as in Fe. In such a spin $S = 2$ system, the longitudinal tip–magnetic field gradient drives EPR, in contrast to $S = 1/2$ systems such as TiH, where the transverse tip–magnetic field gradient causes EPR excitations. Our theory also predicts nonlinear driving forces through coupling to induced electric dipoles, which potentially opens this technique to the investigation of nonpolar systems.

RESULTS

Recording EPR spectra with an STM

Our EPR-STM setup is depicted in Fig. 1A: A spin-polarized tip is positioned above a magnetic adatom adsorbed on a double layer of MgO on Ag(100) (*10*). A magnetic field splits the atomic energy levels by the Zeeman interaction, and a resonant rf excitation induces transitions between these split states. EPR spectra are acquired by sweeping the out-of-plane $\mathbf{B}_{ext}$ while keeping the frequency $\omega_{rf}/2\pi$ constant and detecting the rf-induced change in the dc tunneling current ΔI using a modulation scheme of the rf source, followed by a lock-in detection (*10*). Figure 1B shows typical constant frequency EPR spectra on Fe and TiH. Following (*4*), EPR is detected electrically through the tunneling magnetoresistance (TMR) of the tip-adatom junction. Because the conductance of the STM junction depends on the relative alignment of the magnetic moments of the tip and adatom, the EPR dynamics induces a change of both the dc and ac TMR. The dc TMR variation is caused by the time-averaged population change of the magnetic adatom states and is detected as a change of the dc tunneling current. The ac TMR originates from the rf conductance change and gives rise to an additional (homodyne) dc tunneling current via mixing with the rf voltage. For further experimental details, see Materials and Methods and (*10*).

To discriminate between different EPR mechanisms, we first have to characterize the basic elements of an EPR-STM experiment, i.e., the rf excitation, the EPR species, and the magnetic tip. The rf excitation is provided by an antenna capacitively coupled to the STM tip and is well understood from a previous study (*10*). In addition, Fe and TiH adatoms are two well-known, yet magnetically distinct systems (*1*, *2*, *10*). However, the structure of the magnetic tip is completely unknown and requires further characterization. To this end, we record an extensive EPR dataset on the Fe and TiH adatoms as shown in Fig. 1A using the same magnetic microtip at a similar external magnetic field, resulting in 119 spectra in the EPR-STM parameter space (see Fig. 2). Note that spectra for different V_{rf} values are offset for better visibility in Fig. 2 (C to D). Without any further analysis, these spectra already reveal important characteristic features of EPR-STM: (i) The amplitude and width of the EPR signal of both magnetic adatoms grow with increasing rf voltage amplitude V_{rf} and decreasing standoff distance s, indicating that the excitation is stronger close to the tip. (ii) The external magnetic field at resonance changes by less than 20 mT with either s or V_{rf}, ruling out tip and bias-induced changes of the electronic ground state of the probed magnetic adatoms. (iii) The peak-to-peak amplitude is about twice as large for TiH as for Fe. (iv) The EPR spectra of TiH have opposite sign than those of Fe (note that the Fe spectra are inverted in Fig. 2, A and C), and (v) the EPR signal line shape of TiH has a stronger dependence on s than that of Fe. (vi) The EPR signal is mostly symmetric for Fe and more asymmetric for TiH, for which the asymmetry grows with increasing V_{rf}. The same general features are observed when changing the STM tip, for all the six different EPR-active microtips investigated in this study (see fig. S9). These observations indicate a different nature of EPR-STM for Fe and TiH, requiring a more detailed analysis of the recorded spectra to allow for an assessment of the EPR driving forces.

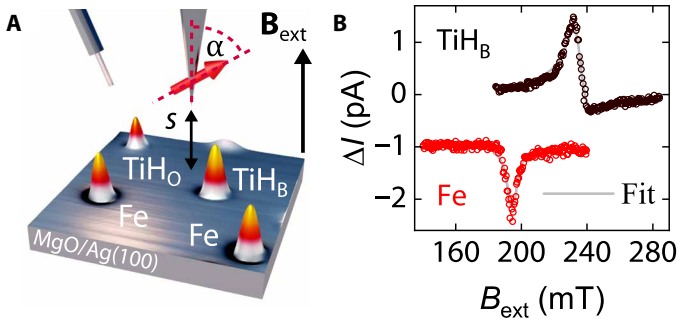

Fig. 1. Principle of EPR-STM and representative EPR spectra. (**A**) Schematic of the STM junction showing single magnetic adatoms on a double-layer MgO on Ag(100) driven by an rf antenna using a spin-polarized tip. The tip is at a standoff distance s from point contact with the surface. The tip magnetization makes an angle α with respect to the out-of-plane external magnetic field B_{ext}. The schematic includes a three-dimensional rendering of a constant-current STM image (10 nm by 10 nm) of Fe and TiH adatoms, on which all EPR measurements are performed (subscripts O and B label apical and bridge binding sites relative to the oxygen lattice, respectively). Set point current, 50 pA; dc bias, 30 mV. (**B**) Representative EPR spectra measured by sweeping B_{ext} on TiH_B and Fe adatoms shown in (A) (left Fe adatom) while applying an rf voltage to the antenna. The solid lines are fits to the data (see main text). A nonresonant background is subtracted from both spectra; for clarity, the Fe spectrum is offset by −1 pA. Settings: $I_{dc} = 70$ pA, $V_{dc} = 160$ mV, $V_{rf} = 256$ mV, and $\omega_{rf}/2\pi$: 8 GHz for Ti_B and 36 GHz for Fe.

Analysis of the EPR spectra and Rabi rate

For a quantitative analysis of the mechanisms that drive the EPR of Fe and TiH, we fit the spectra in Fig. 2 using a general model of the change in tunneling current flowing between a magnetic adatom and a spin-polarized tip in the presence of an rf bias. According to (*4*) and as summarized in section S2, the total rf-induced current is given by

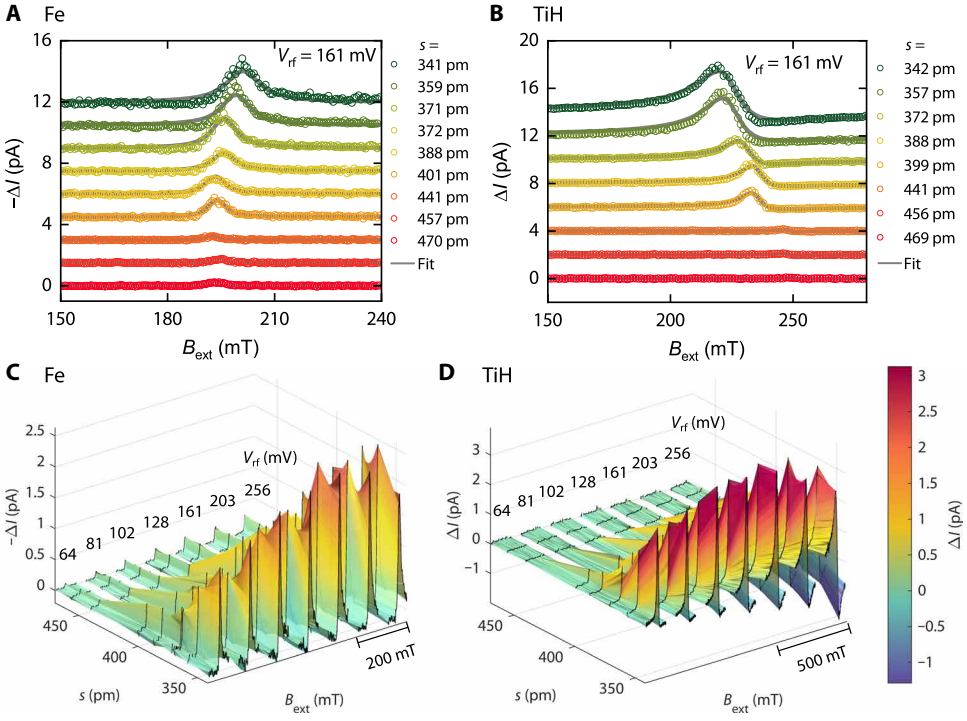

Fig. 2. EPR dataset on Fe and TiH. EPR spectra of Fe at $\omega_{rf}/2\pi$ = 36 GHz (**A** and **C**) and TiH at 8 GHz (**B** and **D**) recorded with the same microtip for varying the standoff distance s and rf voltage amplitude V_{rf}. For better visibility, the Fe spectra are inverted. (A) and (B) show data for a constant rf voltage amplitude of V_{rf} = 161 mV. The spectra are vertically offset for better visibility. In (C) and (D), the spectra are offset along the B_{ext} axis for distinct values of V_{rf}. Rows from left to right correspond to V_{rf} = 64, 81, 102, 128, 161, 203, and 256 mV.

$$\Delta I = I_{off} - a_{TMR} I_{dc} \frac{\Omega^2 T_1 T_2}{1 + \Delta\omega^2 T_2^2 + \Omega^2 T_1 T_2} \left(\cos\alpha + \frac{\Delta\omega T_2 V_{rf}}{2\Omega T_1 V_{dc}} \sin\alpha \right) \quad (1)$$

where the first term is an offset that accounts for magnetic field–independent rectified rf currents due to STM junction conductance nonlinearities. The second term describes the TMR of the STM junction modulated by spin precession. It includes a term proportional to the time-averaged projection of the atomic magnetic moment on the tip magnetization ($\sim \cos\alpha$) and a homodyne contribution ($\sim \sin\alpha$), where α is the angle between the tip magnetization and the external magnetic field (see Fig. 1A). a_{TMR} is a parameter that describes the TMR amplitude, and I_{dc} is the dc set point current. Note that, for a vanishing V_{dc}, the ratio I_{dc}/V_{dc} that appears in the second term approaches the dc set point conductance of the tunneling junction. T_1 and T_2 are the longitudinal and transverse spin lifetimes, respectively, and $\Delta\omega = 2\mu(B_{ext}^0 - B_{ext})/\hbar$ is the detuning from the external magnetic field at which the resonance occurs B_{ext}^0, with $\hbar$ as the reduced Planck constant and μ as the adatom magnetic moment. The latter is 1 μ_B for TiH (*10*) and 5.2 μ_B for Fe (*27*).

Equation 1 was initially derived for a S = 1/2 system such as TiH, but we show below that it is also valid for higher spin systems such as Fe if the Rabi frequency Ω of an effective two-level system is appropriately renormalized by the matrix element connecting the true initial and final magnetic states, as outlined in section S2. We also note that Eq. 1 neglects a possible spin torque initialization of the magnetic adatom spin (*5*), which would alter the EPR signal through a change of the off-resonant magnetic state population induced by inelastic spin-flip excitations by the tunneling electrons. The impact of this effect is minimized by measuring the EPR in a relatively narrow range of the dc bias voltage with constant polarity and using rf voltage amplitudes large compared to the inelastic spin-flip thresholds. Last, our model neglects the hyperfine interaction (*11*), which is justified because the investigated adatoms did not show an associated broadening or splitting of the EPR lines.

Given that all the spectra in Fig. 2 were acquired with the same tip, we perform a simultaneous fit of the entire set of EPR spectra based on the following assumptions: The magnetic moments of the probed adatoms are supposed to point on average along the out-of-plane external magnetic field $\mathbf{B}_{ext}$ (see Fig. 1A), which is justified for Fe owing to its large out-of-plane anisotropy (*27*) and for the isotropic TiH moment if $\mathbf{B}_{ext}$ is dominant with respect to in-plane components of the tip-induced magnetic field (*2*). We assume that the tunneling electrons are the main source of T_1 and T_2 events due to the large values of the dc and the rf current (see fig. S3A) as also previously observed (*5*, *28*). Thus, we set $T_{1,2} = e/(r_{1,2}I)$, where $r_{1,2}$ is the probability that a single tunneling electron induces a $T_{1,2}$ event and I is the total current given by the sum of the dc and the root mean square rf current I_{rf}, which is obtained via the dc STM junction conductance (see Materials and Methods). We further account for a fixed increase in EPR spectral line width through a convolution of the EPR spectra with a 4-mT broad Gaussian. This broadening is caused by the atom-tracking scheme, in which the tip circles atop the magnetic adatom (3 mT; as deduced from typical magnetic field gradients) and by the finite B_{ext} sweep rate (1 mT) (*10*). With these assumptions, we fit all the EPR spectra with Eq. 1 using an adatom-independent value of α, adatom-specific parameters $a_{TMR}^{Fe,Ti}$, $r_1^{Fe,Ti}$, and $r_2^{Fe,Ti}$, and adatom-specific local parameters $B_0^{Fe,Ti}$, $I_{off}^{Fe,Ti}$, and $\Omega^{Fe,Ti}$ that depend

additionally on I_{dc}, V_{dc}, and V_{rf} (see Materials and Methods for further details). The best fit of all the 119 EPR spectra is found for $\alpha = (64 \pm 2)°$, $a_{TMR}^{Fe} = 0.043^{+0.003}_{-0.004}$, $r_1^{Fe} = 6^{+2}_{-1} \cdot 10^{-9}$, $r_2^{Fe} = 0.99^{+0.33}_{-0.24}$, $a_{TMR}^{Ti} = -0.70^{+0.04}_{-0.05}$, $r_1^{Ti} = 0.032^{+0.003}_{-0.003}$, and $r_2^{Ti} = 1.00^{+0.21}_{-0.04}$ (see Fig. 1B, fig. S4, and section S3). Thus, for the relaxation times, we find that nearly every tunneling electron induces a T_2 event, whereas only a small fraction of them leads to a T_1 relaxation, in agreement with previous reports for Fe (*5*). For TiH, on the other hand, a difference in T_1 and T_2 can arise from the different probabilities for inelastic and elastic scattering events of the spin-polarized tunneling electrons with the adatom's spin. Note that our model neglects relaxation mediated by phonons that play a minor role because of the relatively high tunneling currents and the thin MgO support (*28*). The opposite sign of a_{TMR} for Fe and TiH reflect the opposite polarities observed in the raw data (Figs. 1B and 2).

From the above fit parameters, we derive three important quantities, namely, the line width $\sqrt{1+\Omega^2 T_1 T_2}/(\pi T_2)$ (Fig. 3, A and B), the spectral amplitude $a_{TMR} I_{dc} \Omega^2 T_1 T_2/(1+\Omega^2 T_1 T_2)$ (Fig. 3, C and D), and the asymmetry $T_2 V_{rf}/(2\Omega T_1 V_{dc})$ (fig. S6A). We observe that the line width grows almost linearly with the rf voltage amplitude V_{rf} at constant I_{dc}, which is a consequence of being in the strong-driving regime, i.e., $\Omega^2 T_1 T_2 \gtrapprox 1$. This is consistent with the saturated amplitude for Fe for all V_{rf} and with the saturating amplitudes for TiH at the two lowest values of I_{dc} (see Fig. 3, C and D). For TiH and the highest value of I_{dc} = 120 pA, that is for the smallest standoff distance s, we do not observe saturation of the amplitude at large V_{rf}. This finding might indicate a change of the TiH magnetization orientation due to an increased magnitude of the in-plane tip–magnetic field that is not included in our analysis. The asymmetry of the EPR signal of TiH (fig. S6B) grows linearly with V_{rf} and strongly depends on I_{dc} reflecting the intricate dependence of the Rabi rate on I_{dc} discussed below. Fe spectra show nearly symmetrical line shapes and accordingly have vanishing asymmetries (fig. S6A), which is consistent with previous studies (*5*) and can be understood by the long T_1, i.e., small r_1 of Fe compared to TiH. In essence, this difference arises because a tunneling electron can induce a direct transition in TiH, which corresponds to a spin excitation with $\Delta S = 1$, whereas Fe has a large spin and orbital moment that cannot be directly excited by a single electron. The long T_1 of Fe suppresses the asymmetric EPR line shape originating from the homodyne component of Eq. 1. The shorter T_1 of TiH, on the other hand, gives an asymmetric line shape as also reported previously (*2*). Last, the experimental Rabi rate Ω is given in Fig. 3 (E and F) and ranges from about 100 MHz for TiH to about 1 MHz for Fe, consistent with the literature (*12*). This information allows us to perform a qualitative assessment of the different proposed EPR-STM mechanisms, as described below.

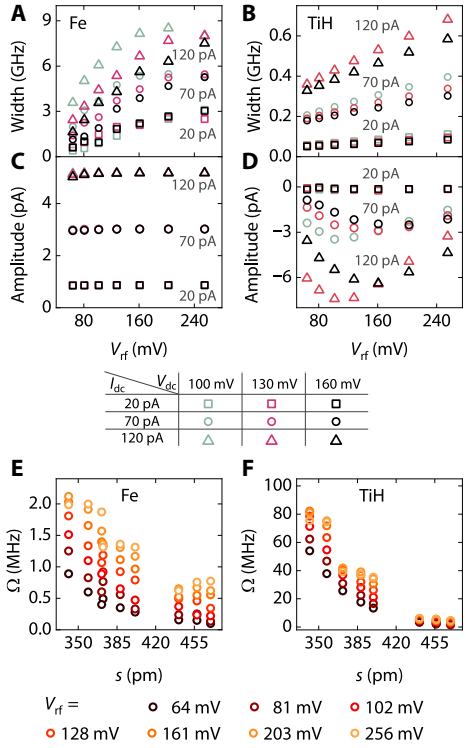

Fig. 3. Amplitude and width of the EPR spectra and experimental Rabi rates. A fit of all 119 EPR spectra using Eq. 1 (see main text, section S3, and fig. S4) allows for calculating the spectral line widths (**A** and **B**) and amplitudes (**C** and **D**) for varying rf voltage amplitude V_{rf}, dc voltage V_{dc} and set point current I_{dc}. In (C), most symbols for a given I_{dc} overlap. Experimental Rabi rate Ω versus standoff distance s for Fe (**E**) and TiH (**F**) at different V_{rf} values. The errors in (E) to (F) of ±2% are smaller than the size of the symbols.

Assessment of different EPR-STM mechanisms

We now contrast the observations summarized in Figs. 2 and 3 with the expectations for different excitation models of EPR-STM.

1) A Rabi rate Ω induced by the ac magnetic field originating from the rf tunneling current and the rf displacement current has been discarded previously by estimating the respective magnitudes (*7*, *10*). In addition, we note that both contributions should not depend strongly on the standoff distance s, contrary to our measurements (see Fig. 2). Moreover, the rf magnetic field caused by the displacement current should depend monotonically on s, unlike what we observe for Fe in Fig. 3E. In addition, the displacement current should be proportional to the frequency ω_{rf}, which is not consistent with EPR measurements performed at different ω_{rf} values.

2) A spin torque–mediated EPR (*24*) is expected to be proportional to I_{rf} and independent of s. Such a mechanism is unlikely, given the strong dependence of Ω on s at constant dc set point current (see fig. S6, E and F).

3) A purely rf electric field–driven EPR-STM, in which rf-induced spin-polarized tunneling electrons couple via the exchange interaction to the adatom magnetic moment, has been proposed in (*20*). This coupling can be understood as a current-induced effective magnetic field driving the EPR. However, this mechanism can be discarded because it fails to explain EPR in half-integer spin systems such as TiH.

4) A change of the crystal field caused by adatom vibrations induced by the rf electric field (*1*, *22*) should yield a Rabi rate that depends monotonically on s, unlike what is observed for Fe in Fig. 3E. Moreover, our multiplet calculations (see Fig. 4, Materials and Methods, section S6, and fig. S8) indicate that the crystal field operators yield vanishing EPR driving forces for Fe. Nevertheless, rf-induced variations of the crystal field could yield minor contributions to the Rabi rate in the case of TiH.

5) A modulation of the density of states by the precessing spin of the magnetic adatom mediated by spin-orbit coupling (*19*) can be ruled out because it should be observable even with a nonmagnetic tip. This is not observed experimentally and is inconsistent with the

results presented in Fig. 5 (A and B), which show that the resonance field depends on the distance between the magnetic tip and the EPR species.

6) A modulation of the *g*-factor anisotropy of the EPR species by the vibrations induced by the rf electric field should lead to a Rabi rate that depends monotonically on *s* because the driving electric field is proportional to 1/*s* in a simple plate capacitor model (*25*). This is in contrast with our experimental findings for Ω shown in Fig. 3E.

7) In the PEC model (*22*), Ω is expected to be proportional to the conductance of the STM junction if the adatom-tip interaction is dominated by the exchange interaction (*8*). This prediction is partly inconsistent with our experimental Ω (see fig. S6, C and D), which might indicate an additional tip-adatom interaction such as dipolar coupling (see below). Apart from that, the PEC mechanism implies complex dependencies of Ω on the experimental parameters I_{dc}, V_{dc}, *s*, and V_{rf} (*7*) that require a quantitative evaluation.

8) A cotunneling mechanism (*23*) and an open quantum system approach (*26*) have been proposed to describe the excitation and detection of EPR, respectively. Testing these approaches requires a detailed knowledge of the wave functions of the tip and EPR species that is experimentally difficult to obtain. However, as we will discuss later, these approaches represent more general descriptions that include some of the other mechanisms.

On the basis of this analysis, we conclude that mechanisms (1 to 6) are not compatible with our experimental dataset. Further evaluation of (7) and of EPR-STM in general requires quantitative knowledge of the involved transition matrix elements and of the total magnetic field acting on the EPR species. We focus here on the most relevant magnetic moment operator mediating EPR (see below) but discuss further operators in section S6. Our analysis goes beyond an ideal $S = 1/2$ system because EPR encompasses a much larger variety of magnetic complexes with $S > 1/2$. It is thus important to determine what drives the EPR of Fe on MgO, which is known to have $S = 2$ (*27*), to reach a comprehensive understanding of EPR-STM.

Transition matrix elements of EPR-STM for atoms with *S*>1/2

To drive EPR, we consider a perturbative oscillating magnetic field $\mathbf{B}_1$ acting on the magnetic adatom. The $\mathbf{B}_1$ field interacts with the magnetic moment of the adatom $\hat{\boldsymbol{\mu}} = -\mu_B(\hat{\mathbf{L}} + 2\hat{\mathbf{S}})/\hbar$ via the Zeeman interaction, and the corresponding interaction Hamiltonian reads $H' = \mu_B(\hat{\mathbf{L}} + 2\hat{\mathbf{S}})\cdot\mathbf{B}_1/\hbar$, where $\hat{\mathbf{S}}$ and $\hat{\mathbf{L}}$ are the spin and orbital angular momentum operators, respectively. In the derivation of Eq. 1 for single TiH adatoms, $\mathbf{B}_1$ was assumed to be transverse to the static magnetic field $\mathbf{B}_0$ inducing the Zeeman splitting of the adatom's states, as in the standard two-level model of EPR [(*4*) and section S2]. This assumption, however, has not been tested in detail and (*4*) makes no predictions about the requirements on $\mathbf{B}_1$ to drive EPR in Fe. For TiH on the bridge binding site (see Fig. 1A), we assume a nearly perfect physical $S = 1/2$ system due to the low binding site symmetry. Accordingly, the two lowest states $|0\rangle$ and $|1\rangle$ are the *LS*-basis states $|M_L = 0, M_S = \pm 1/2\rangle$ with quenched orbital moment, as reported previously (*2*, *10*). Those states are the natural eigenstates of the $\hat{\mathbf{L}}$ and $\hat{\mathbf{S}}$ operators and the interaction Hamiltonian becomes $H' = \frac{2\mu_B}{\hbar}(\hat{S}_x B_{1,x} + \hat{S}_y B_{1,y} + \hat{S}_z B_{1,z})$. Because $\hat{S}_z$ is diagonal in the $|M_L = 0, M_S = \pm 1/2\rangle$ basis, it is evident that only transverse $\mathbf{B}_1$ fields can drive a transition between $|0\rangle$ and $|1\rangle$. For instance, for a transverse $\mathbf{B}_1$ field along *x*, the off-diagonal matrix element that drives the transition is $H'_{01} = \mu_B B_{1,x}(t)$ because $\hat{S}_x = \frac{\hbar}{2}\hat{\sigma}_x$ with $\hat{\sigma}_x$ being the *x* component of the vector of Pauli matrices $\hat{\boldsymbol{\sigma}}$. Note that the transverse field oscillates in time proportionally to $\cos\omega_{rf}t$, i.e., $B_{1,x}(t) = B_{1,x}\cos\omega_{rf}t$ and that its amplitude relates to the Rabi rate according to $\hbar\Omega = \mu_B B_{1,x}$.

The situation is more complex for Fe, which has a state multiplicity of 5 due to the effective spin $S = 2$, and the presence of strong orbital moments (see Fig. 4A). At zero magnetic field, the ground-state doublet is separated by about 14 meV from the next excited doublet (*27*). Therefore, only the two lowest states are thermally occupied in the range of temperature and magnetic field probed by our experiments. Transitions to higher doublets are too high in energy to be driven by the rf excitation. This renders Fe also an effective two-level system. Within this effective two-level system, we need to evaluate the interaction Hamiltonian H' in the eigenstate basis $|0\rangle$ and $|1\rangle$, which are a general superposition of the $|M_L, M_S\rangle$ basis wave functions. To describe the states $|0\rangle$ and $|1\rangle$, we use the wave functions obtained from a multiplet model that was successfully used to simultaneously describe the x-ray absorption spectral line shape and the low-energy excitations of Fe/MgO probed by STM (*27*). We find that the off-diagonal matrix elements H'_{01} are proportional to $B_{1,z}$, whereas the in-plane field components, $B_{1,x}$ and $B_{1,y}$, yield vanishing matrix elements (see Materials and Methods and section S6 for more details). That is, only the *z* component of the magnetic moment operator yields an off-diagonal matrix element $\langle 1|\hat{L}_z + 2\hat{S}_z|0\rangle \neq 0$. This is known in EPR spectroscopy to be the case for integer spins where longitudinal $\mathbf{B}_1$ fields are used to drive the EPR transition (*29*). Further, the matrix element is strongly dependent on the Zeeman-splitting field B_0, as shown in Fig. 4B. Fe behaves as an integer-spin system, in which the levels are strongly intermixed by the crystal field and spin-orbit interaction (Fig. 4C). This leads to wave functions that are not eigenfunctions of the Zeeman Hamiltonian; thus, the composition of the states $|0\rangle$ and $|1\rangle$ changes with the external magnetic field. Setting again $\hbar\Omega$ equals to the amplitude of H'_{01}, we see that the Rabi rate Ω, besides being proportional to the *z* component of the $\mathbf{B}_1$ field, is also proportional to the matrix element $\langle 1|\hat{L}_z + 2\hat{S}_z|0\rangle$.

Further, we describe the effective two-level system for Fe, not in terms of the magnetic moment operator, but by the two-level polarization operator $\hat{\mathbf{P}} \propto \hat{\boldsymbol{\sigma}}$ (see section S6). Following this approach, we can model the two EPR species using the same model for the tunneling current while taking into account that the origin of the Rabi rate is different for the two species. We derive the Bloch equations

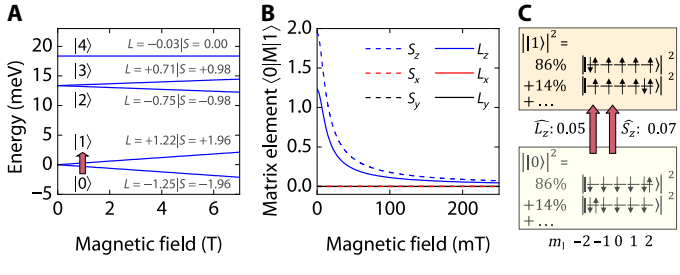

Fig. 4. Energy levels and EPR matrix elements of Fe/MgO/Ag(100). (**A**) Calculated lowest energy levels of Fe obtained from the multiplet theory for an out-of-plane magnetic field ranging from 0 to 7 T. (**B**) Calculated components of the matrix elements of the orbital and spin momentum operator $\hat{\mathbf{L}}$ and $\hat{\mathbf{S}}$, respectively, for an external magnetic field along *z*. Note that apart from the operators S_z and L_z, all other matrix elements are $<10^{-14}$. (**C**) Schematic of the transition matrix elements between the EPR-active states $|0\rangle$ and $|1\rangle$ represented in the orbital momentum basis m_l. Wave function contributions below 1% are omitted.

in terms of the polarization vector $\hat{\mathbf{P}}$ with a driving term proportional to $\hat{P}_x$ and with an effective driving field strength given by $\mu_B\langle 1|\hat{L}_z + 2\hat{S}_z|0\rangle B_{1,z}/\hbar$. Moreover, in the evaluation of the TMR for the read out of the EPR signal in the STM junction, we use the polarization vector $\hat{\mathbf{P}}$ instead of the physical magnetic moment of the system (see section S2) because the conductance of the STM junction should only depend on the occupation and coherence of the involved EPR states (*26*). This approach reflects the fact that the conductance of the STM junction depends on the nature of the magnetic adatom states and not only on the associated magnetic moment. Note that, for a real $S = 1/2$ system, the polarization operator is identical to the spin operator.

Thus, we obtain formally the same equation, Eq. 1, for the experimentally detected EPR signal for the two EPR species, Fe and TiH. However, the physical interpretation of the effective driving field component and strength that yield Ω differs for the two cases. In summary, our analysis shows that EPR in systems with $S > 1/2$ can be driven by STM, provided that longitudinal field gradients are nonzero. Note that the small in-plane magnetic field component of the tip produces negligible matrix elements for the in-plane magnetic moment operator as compared to its z component (see fig. S8).

Magnetic field acting on the adatoms

At the position of the EPR species, the total magnetic field is the sum of the external magnetic field $\mathbf{B}_{ext}$ and the tip-induced effective magnetic field $\mathbf{B}_{eff}$. Quantitative analysis of the Rabi rate requires estimation of $\mathbf{B}_{eff}$ acting on the EPR species. Here, we determine $\mathbf{B}_{eff}$ by considering the measured resonance positions B^0_{ext}, i.e., the value of $\mathbf{B}_{ext}$ at resonance, as shown in Fig. 5 (A and B). The intrinsic resonance position in the absence of a tip-induced magnetic field is given by $2\hbar\omega_{rf}/\mu$, which yields 247 mT for Fe at $\omega^{Fe}_{rf}/2\pi = 36$ GHz and 286 mT for TiH at $\omega^{Ti}_{rf}/2\pi = 8$ GHz. The measured EPR resonance position deviates from these values as a function of the standoff distance s. These deviations are caused by the finite $\mathbf{B}_{eff}$ produced by the tip. The upturn of B^0_{ext} at $s \approx 420$ pm for Fe indicates that the magnetic force changes from attractive to repulsive upon approaching this specific tip (Fig. 5A), which is unexpected if the interaction only contains an exchange contribution as determined in previous studies (*2*, *7*, *8*). This finding indicates that the tip magnetic field comprises two competing terms, which we assume to be an exchange field $\mathbf{B}_{xc}$ and an additional dipolar field $\mathbf{B}_{dip}$. These two fields were shown to be present independently from one another for certain STM tips in (*6*) and were also discussed but not taken into account simultaneously in (*4*). We note that previous studies using an atomic force microscope with a magnetic tip (*30*) have shown that the exchange interaction might change sign depending on the overlap of the tip and the magnetic adatom wave functions. Here, however, we find that the dipolar field in addition to an exponentially decaying exchange field is sufficient to account for the observed change of $\mathbf{B}_{eff}$ without considering more complex exchange regimes. Given the cylindrical symmetry of the STM junction, it is sufficient to determine the x and z components of $\mathbf{B}_{eff}$, which can be written as (*22*)

$$\mathbf{B}_{eff} = \begin{pmatrix} B_{xc,x} + B_{dip,x} \\ B_{xc,z} + B_{dip,z} \end{pmatrix} = \begin{pmatrix} \left(a\, e^{-s/\lambda_{xc}} - \frac{b}{s^3}\right)\sin\alpha \\ \left(a\, e^{-s/\lambda_{xc}} + \frac{2b}{s^3}\right)\cos\alpha \end{pmatrix} \quad (2)$$

where a is the exchange parameter, b is the dipolar parameter, s is the tip standoff distance defined through point contact between the tip and the magnetic adatom (see Materials and Methods), and λ_{xc} is the exchange decay length. Note that we orient the coordinate system such that $B_{eff,y} = dB_{eff,y}/ds = 0$ along the z axis and for $x = 0$. We fit $B^0_{ext}(s)$ using $B_{eff,z} + 2\hbar\omega_{rf}/\mu$ (see Eq. 2) with a fixed $\alpha = 64°$ as determined above and find a good agreement between experiment and theory for $\lambda^{Fe}_{xc} = (370 \pm 60)$ pm, $a^{Fe} = (-0.6 \pm 0.1)$ T, $\lambda^{Ti}_{xc} = (170 \pm 20)$ pm, $a^{Ti} = (-2.2 \pm 0.1)$ T, and $b = (0.2 \pm 0.03)\mu_0\mu_B$ (see Fig. 5, A and B). The parameter b implies a tip magnetic moment of about 3 μ_B, which is reasonable, given that few Fe atoms form the tip apex. The values for a compare well with reports of the exchange field, ranging from 0.1 to 10 T for similar systems (*4*, *7*, *31*). For all six tips used within this work (see fig. S9), we find values of $a < 0$ independent of the adatom. The values for λ_{xc} are somewhat larger than reported values (*4*, *7*, *31*), but λ_{xc} is expected to strongly depend on the detailed atomic structure of the microtip. In this way, we completely characterize $\mathbf{B}_{eff}$ for this magnetic microtip, which is shown for Fe in Fig. 5C, assuming an isotropic exchange interaction. This allows us to derive the corresponding magnetic field gradients along z as shown in Fig. 5D containing substantial contributions from dipolar and exchange tip-adatom interactions at the same time.

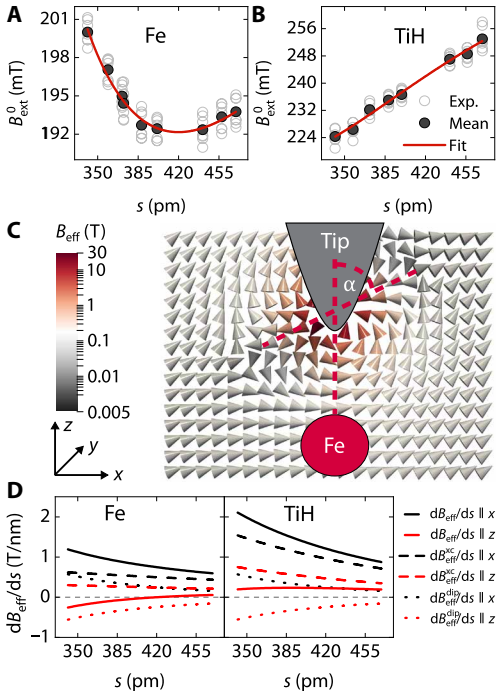

Fig. 5. Characterization of the tip magnetic field. Measured resonance field B^0_{ext} versus standoff distance s for Fe (**A**) and TiH (**B**). Solid lines are fits based on Eq. 2. (**C**) Cross-sectional view of the effective tip magnetic field $\mathbf{B}_{eff}$ experienced by the Fe atom at different locations with respect to the STM tip deduced from Eq. 2 assuming an isotropic exchange interaction. The cross section is a cut along the tip-atom plane with dimensions of 0.8 nm by 0.6 nm. (**D**) Gradient of the effective magnetic field $d\mathbf{B}_{eff}/ds$ along x and z versus standoff distance s for Fe (left) and TiH (right) with the corresponding dipolar (B_{dip}) and exchange (B_{xc}) contributions. The gradients along y vanish.

Quantitative evaluation of the PEC Rabi rate and comparison with experiment

Knowledge of the transition matrix elements and $\mathbf{B}_{eff}$ is essential to compute the Rabi rate expected for the PEC model [see section S2 and (*22*)], which is given by

$$\Omega_{\mathrm{PEC}}^{\mathrm{Fe,TiH}} = \left| \frac{\mu_B}{\hbar} \Delta z_{\omega_{\mathrm{rf}}} \frac{\mathrm{d}\mathbf{B}_{\mathrm{eff}_{z,x}}}{\mathrm{d}s} \langle 1 | \hat{\mathbf{L}} + 2\hat{\mathbf{S}} | 0 \rangle \right| \quad (3)$$

Here, different components of the magnetic field gradient drive Fe and TiH as discussed above. In more detail, the field that drives EPR is given by $B_1^{\mathrm{Fe}} = \Delta z_{\omega_{\mathrm{rf}}}^{\mathrm{Fe}} \mathrm{d}B_{\mathrm{eff}_z}^{\mathrm{Fe}}/\mathrm{d}s$ and $B_1^{\mathrm{TiH}} = \Delta z_{\omega_{\mathrm{rf}}}^{\mathrm{TiH}} \mathrm{d}B_{\mathrm{eff}_x}^{\mathrm{TiH}}/\mathrm{d}s$, where $\Delta z_{\omega_{\mathrm{rf}}}$ is the amplitude of the magnetic adatom displacement induced by the rf electric field between tip and adatom. To compute $\Delta z_{\omega_{\mathrm{rf}}}$, we calculate the structural response of the adatoms to a static electric field applied normal to the surface by means of density functional theory (DFT) (for details of the calculations see Materials and Methods). Because the adsorbate species Fe and TiH form a polar bond to the MgO substrate, an external electric field can displace the adatoms and vary the length of the bond to the surface. As the frequencies of the local vibrational modes of the adatoms lie at several terahertz [see Materials and Methods, fig. S7, and previous work (*7*)], we expect $\Delta z_{\omega_{\mathrm{rf}}}$ to adiabatically adjust to the gigahertz electric fields, justifying our static approach in the calculations. As seen in Fig. 6 (A and B), the Fe and Ti adatoms are both displaced by about 0.5 pm/(V/nm) but in opposite directions. The opposite response appears as a 180° phase change in the driving terms and has no consequences for the measurements. Note that the inverted EPR spectra of Fe and TiH instead originate from the sign change in a_{TMR}. We observe that the displacement does not depend linearly on the electric field but follows a second-order polynomial (see also fig. S7). This result is rationalized by noting that the linear response is due to the coupling to permanent electric dipoles, whereas the second-order term arises from a coupling to induced electric dipoles that has (refers to "a coupling") not been reported before (*7*). Last, $\Delta z_{\omega_{\mathrm{rf}}}$ is obtained by considering only the terms oscillating at the fundamental frequency ω_{rf} derived from the second-order polynomial fit of the displacement (see Fig. 6, A and B), i.e., neglecting time-independent offsets and terms oscillating at $2\omega_{\mathrm{rf}}$, and using the experimental electric field $E = [V_{\mathrm{dc}} + V_{\mathrm{rf}} \cos(\omega_{\mathrm{rf}} t)]/s$ (see section S5).

After these steps, we can lastly compute the PEC Rabi rate Ω_{PEC} using Eq. 3, as shown in Fig. 6 (F and G). We find that the calculated values of Ω_{PEC} match the experimental Rabi rate Ω reported in Fig. 3 (E and F) for TiH and only deviate by a factor of 2 for Fe. Notably, Ω_{PEC} describes the $\Omega(s)$ dependence adequately for Fe, i.e., changing from decreasing to slightly increasing at $s \approx 420$ pm. This change in slope arises from the differences in the distance dependence of the exchange and dipolar interactions with the adatom. In addition, for TiH, the decreasing trend of Ω with s is reproduced correctly. Discrepancies in the magnitude are ascribed to an inaccurate determination of the electric field, which was shown to deviate from the plate capacitor model used here (*32*). Moreover, keeping the adatom magnetic moment fixed along z is especially critical for TiH at small standoff distances and can lead to errors. Last, including a finite phase between driving field and the precessing magnetic adatom spin, as well as a bias-dependent TMR and a spin-torque initialization (*5*) could further improve the agreement with the experiment.

DISCUSSION

Given the limitations of our model, the overall good agreement between experiment and theory shows that the PEC mechanism allows for a consistent interpretation of EPR-STM spectra provided that the matrix elements of the EPR transitions and the different components of the magnetic field gradients are properly accounted for. Crucially, we find that in $S = 1/2$ systems, such as TiH, the rf magnetic field perpendicular to the magnetic moment drives EPR, whereas for the more complex $S = 2$ Fe system, we find a different driving force, i.e., the rf magnetic field along the static magnetic field. This finding reflects the fact that transitions between states with spin quantum numbers $m_S = \pm 2$ as in Fe imply a change in spin angular momentum of $4\hbar$ and are therefore magnetic dipole–forbidden, i.e., cannot be driven by a transverse rf magnetic field because the rf photons can only provide $1\hbar$. Instead, these transitions are enabled by the mixing of the ground and first excited state as found in Fe (*27*), which allows for a longitudinal rf magnetic field to drive EPR. These distinct EPR driving forces for transitions that are magnetic dipole–forbidden have also been observed in ensemble EPR measurements (*29*), where they are known as longitudinal or parallel polarization EPR.

The larger EPR amplitudes measured for TiH compared to Fe are mainly caused by the 10 times larger EPR transition matrix element of TiH and the increasing weight of the homodyne detection channel with increasing V_{rf} as compared to Fe, where this detection channel is ineffective because of the larger T_1.

As mentioned previously, the PEC mechanism can be understood as a special case of an EPR theory involving a cotunneling picture (*23*). In that mechanism, the rf electric field alters the tunneling barrier

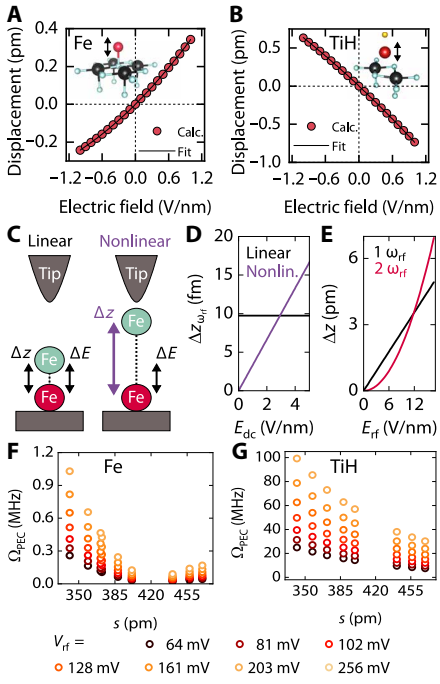

Fig. 6. Adatom displacement induced by the electric field in the STM junction and calculated Rabi rate. (**A** and **B**) Detail of the atomic arrangement used for the DFT calculations of Fe (A) and TiH (B) and calculated displacement versus static out-of-plane electric field. Color code: Mg (black), O (light-blue), Ti (red), H (yellow), and Fe (purple). (**C**) Schematic of linear and nonlinear displacements Δz due to the applied electric field ΔE. (**D**) Calculated linear and nonlinear displacement for Fe at the radio frequency $\Delta z_{\omega_{\mathrm{rf}}}$ versus dc electric field E_{dc} for $V_{\mathrm{rf}} = 10$ mV. (**E**) Calculated displacement Δz for Fe versus rf electric field E_{rf} for $V_{\mathrm{dc}} = 10$ mV at the fundamental frequency ω_{rf} and the second harmonic frequency $2\omega_{\mathrm{rf}}$ of the driving rf field. Standoff distance is 300 pm for (D) and (E). (**F** and **G**) Calculated Rabi rate Ω_{PEC} versus standoff distance s for Fe (F) and TiH (G) deduced from Eq. 3.

that can be effectively mapped onto a time-dependent overlap of adatom and tip wave functions, which accounts also for a time-dependent exchange coupling. Thus, this model includes the PEC mechanism, in which the magnetic adatom vibration causes the magnetic adatom-tip interactions to vary over time. Similarly, the treatment of EPR-STM within an open quantum system approach (*26*) is also not in contradiction with the PEC mechanism. This model accounts for the coupling of the EPR species and spin-polarized tip to reservoirs of energy and angular momentum and, additionally, introduces generalized Bloch equations to explain EPR, consistent with our treatment. However, this approach does not specifically address how the EPR transitions are driven but rather outlines how they are sensed by the tunneling current in the experiment. Thus, these concepts can be combined with the theory used in this work to yield a full quantum description of EPR-STM in the future.

Our study also shows that EPR of single Fe atoms is possible at temperatures of 5 K using an out-of-plane external magnetic field, unlike in (*1*, *5*, *6*, *8*, *12*) that used predominantly in-plane fields (see also the discussion on the influence of the magnetic tip in section S1). As indicated by our multiplet calculations, an in-plane magnetic field increases the EPR signal only very weakly (compare with Fig. 4, section S6, and fig. S8, A to C) and is not required in principle. In contrast, we find an optimal out-of-plane magnetic field of about 130 mT that is a compromise between the rapidly decreasing EPR transition matrix element for an increasing out-of-plane magnetic field and the off-resonant population difference between the states $|0\rangle$ and $|1\rangle$ that is proportional to $\tanh(\mu B_0/k_B T)$, where k_B is the Boltzmann constant and $T = 4$ K. Note that spin pumping has been neglected and that considering additionally the dependence of the tip polarization on external field might further increase this optimal magnetic field.

In contrast to previous studies (*2*, *7*), we show that the shift of the resonance magnetic field with the standoff distance is not determined by the orientation of the exchange field $\mathbf{B}_{xc}$ alone. That is, the direction of the shift does not allow discriminating between antiferromagnetic and ferromagnetic exchange coupling of the EPR species and tip. Instead, the shift direction is determined by the interplay between $\mathbf{B}_{xc}$ and the dipolar magnetic field as given in Eq. 2. In addition, we find that the signs of the TMR and of the exchange field do not correlate, which might be caused by different contributing electronic states (*33*).

Our DFT modeling allows for a precise calculation of the magnetic adatom displacements, which are about 0.1 pm at ω_{rf}. More specifically, we find a displacement smaller by a factor of five for the Ti atom in the TiH system compared to previous calculations (*7*) at a standoff distance of 430 pm, a dc bias voltage of 50 mV, and an rf voltage amplitude of 10 mV. This difference highlights the importance of calculating the adatom displacement directly, i.e., without involving harmonic approximations of the computed energy landscape as a function of the external electric field. We demonstrate in Fig. 6 (C and D) how the Rabi rate can be tuned by the dc bias voltage through coupling to induced changes in electric dipoles, which readily account for up to 15% of the Fe displacement in our experiment (see also section S5). In fig. S7, we report additional DFT calculations of the displacement of Fe at larger electric fields that show its strong nonlinear response and highlight again the profound impact of induced electric dipole moments on the magnetic adatom displacement. Such a nonlinear response should also enable the driving of EPR at the second harmonic frequency of the rf field (see Fig. 6E). For experimental parameters that are within reach in future studies, both of these predicted nonlinear driving mechanisms (second harmonic driving at $V_{dc} = 10$ mV, $V_{rf} = 3$ V, and $s = 300$ pm and induced electric dipoles at $V_{dc} = 1$ V, $V_{rf} = 10$ mV, and $s = 300$ pm) outperform their linear counterparts as shown in Fig. 6 (D and E), underlining their potential to drive EPR-STM in a broader range of systems than demonstrated to date.

In summary, our combined experimental and theoretical investigation provides a consistent picture of EPR-STM of transition metal adatoms on MgO. Our analysis also allows for fully characterizing the vector magnetic field of the tip, which is convenient for future EPR-STM studies and other STM studies relying on spin-polarized tunneling (*34*). Whereas EPR-STM measurements have been so far only reported for transition metal atoms on MgO, the observation of adatom displacements under rf excitation arising from induced electric dipoles opens the field of EPR-STM to nonpolar paramagnetic species. Moreover, our conclusions suggest that nonresonant EPR driving via second harmonic generation might be feasible, thus allowing for strict separation of the excitation from the probe in pulsed EPR studies (*12*). This nonlinear driving could also enhance the coupling efficiency when approaching the resonant terahertz frequency of phonons by an rf photon upconversion scheme, which will additionally benefit from reduced losses in signal transmission at lower driving frequencies.

MATERIALS AND METHODS

Experimental design

Measurements are performed using a Joule-Thomson STM from Specs operating at 4.5 K and upgraded for rf capabilities [see Fig. 1A and (*10*)]. V_{rf} is characterized by rectification at an STM junction conductance nonlinearity (see below). The sample is a clean Ag(100) surface on which double-layer MgO islands are grown (Fig. 1B) (*10*). Single Fe and Ti atoms are deposited on the cold sample inside the STM. Residual H_2 gas is known to hydrogenate Ti forming TiH complexes (*2*, *10*). The tip is made from a chemically etched W wire that is dipped into the sample to obtain a sharp apex. Spin contrast is achieved by picking up single Fe atoms. We check for tip changes by scanning the respective area before and after EPR spectra were recorded and by recording an EPR spectrum at the beginning and at the end of a parameter sweep with the same settings. The standoff distance s is calibrated by point-contact measurements, $I_{dc}(z)$ and $z(V_{dc})$ curves (see below). dI/dV spectroscopy is performed by adding a sinusoidal voltage (971 Hz; amplitude of a few millivolts) to the dc bias and using a lock-in technique.

EPR spectra are acquired by sweeping the out-of-plane $\mathbf{B}_{ext}$ at a constant ω_{rf} with a sweep rate of 400 μT/s. We modulate the rf voltage with a square wave at 971 Hz and record the first harmonic of the tunneling current ΔI at the modulation frequency using a lock-in amplifier. During EPR sweeps, the tip circulates above the EPR species at a rate of 383 Hz with a radius of 10 pm to track the adatom. The systematic spread in B^0_{ext} for constant s of about ±1 mT (see Fig. 3, C and D) arises from opposite B_{ext}-sweep directions and the limited Hall probe communication speed.

We choose EPR species separated from other magnetic adatoms by more than 3 nm to minimize magnetic interactions (see Fig. 1B). All EPR sweeps on TiH are recorded on the bridge binding site with respect to the oxygen sublattice; notably, TiH on the oxygen binding site quickly destabilizes upon rf excitation. For each EPR

sweep, a nonresonant reference spectrum is recorded and substracted (see below).

Characterization of V_{rf}

We characterize the rf voltage amplitude at the STM junction by rectification of the rf signal at an STM junction conductance nonlinearity as outlined in (*10*). This procedure is performed at the two frequencies used for EPR sweeps, i.e., at 8 and 36 GHz (see fig. S1, A and B).

Characterization of the standoff distance *s*

The standoff distance is characterized in three steps:

1) We perform point-contact measurements in which we open the feedback at 10 mV dc bias and approach with the tip while recording the dc current. At point contact, a plateau in dc current is reached (see fig. S2, A and B). The extracted point-contact conductances are consistent with reported values for Fe (*28*) and a bridge binding site TiH adatom (*4*). From this measurement, we calibrate the absolute tip height above the adatom. Because the value of conductance at point contact was found to be independent of the microtip to a good approximation, we do not repeat this measurement for each microtip used for EPR because it has a high risk of altering the microtip. This similar conductivity at point contact for different microtips can be expected, given the fact that the adatom-MgO-Ag junction is the current-limiting part.

2) We record $I(z)$ curves for the specific microtip used for EPR sweeps avoiding point contact with a finer resolution than in (1) in the range of interest for the EPR spectra. With the point-contact measurement of (1) and by fitting the data with an exponential, the absolute standoff distance is determined (see fig. S2, C and D).

3) We perform $z(V)$ measurements for the specific microtip used for EPR sweeps at the values of I_{dc} used in the EPR sweeps to account for the rigid shift in standoff distance upon change of V_{dc} (see fig. S2, E and F).

We note that steps (2) and (3) are performed at about 200-mT external magnetic field to match the EPR experimental conditions.

Characterization of the rf current

To account for the rf current–induced relaxation processes correctly, the rf current amplitude has to be characterized. Ideally, this is performed via convoluting the experimental dI/dV curve with a sinusoidal rf voltage of the corresponding amplitude over one period. However, this requires a detailed knowledge of the dI/dV curve, which changes with the set point and the external magnetic field. In fig. S3A, we compare this approach to an approximation, in which the rf current amplitude is computed via Ohm's law using the dc tunneling resistance at the set point. From the very good agreement between the two approaches, we conclude that the latter approach is also valid. Note that the data in fig. S3A are obtained for an additional EPR dataset on TiH for varying I_{dc}, V_{dc}, and V_{rf} shown in fig. S9A.

EPR reference spectra

The background signals in EPR sweeps are caused by rectification of the rf voltage at STM junction conductance nonlinearities (*10*). Some of these nonlinearities are of magnetic origin. This means that they change if either the tip or the adatom change their magnetic polarization. Because our EPR sweeps are performed in field ranges, where neither the adatom nor presumably the tip is fully spin polarized, the rf rectification will depend on the external field. On the other hand, the STM junction conductance also strongly depends on I_{dc}, V_{dc}, and V_{rf}. To account for changes in the conductance nonlinearities, i.e., a change of the tip and atom magnetic polarization, as we sweep the magnetic field, a nonresonant background signal is recorded for each of the 119 EPR spectra. For the Fe adatom, a reference sweep at a constant frequency of 8 GHz is performed (see fig. S3B) that we subtract from the resonant sweep at 36 GHz. To this end, the rf voltage amplitude at 8 GHz is matched to the one at 36 GHz by compensating for the rf transfer function toward the STM junction. For TiH, a similar procedure is applied, but the reference is recorded at 36 GHz, whereas the resonant sweep is performed at 8 GHz (see fig. S3C). Note that for the largest values of V_{rf}, a minor inaccuracy in compensating for the rf transfer function required a rescaling of the reference spectrum by a constant that is close to unity to best match the background of the resonant EPR spectrum before subtraction.

Details of the fit procedure

The best fit of the 119 EPR spectra (see Fig. 2 and fig. S4) to Eq. 1 is obtained by minimizing the root mean square deviation from the normalized EPR signal given by $(\Delta I - I_{off})/I_{dc}$. This accounts for the anticipated large dynamic range in ΔI as a function of I_{dc}, i.e., to improve the fit accuracy for small I_{dc}, for which our model assumptions are most appropriate (see discussion following Equation 1 concerning the moving adatom spin angle at closest distances, i.e. for large I_{dc}).

Further, our model uses, in total, 126 parameters that determine the spectral line shape for 119 EPR spectra, i.e., on average, 1.06 free parameters per spectrum. This demonstrates that we chose a minimized set of parameters considering that a Lorentzian line shape is, in principle, determined by three parameters. See also the discussion on the number of fit parameters in section S2.

To determine the global minimum of the fit, we vary the starting conditions and take the result with the smallest root mean square deviation. Figure S5 shows the resulting deviations for different starting parameters of α. We note that our model yields T_1 times that are larger than reported in previous studies (*5*, *28*), in which an in-plane component of the external field of about 10% was present. In addition, the fact that we assume an atom tracking–induced additional broadening independent of the EPR species can lead to an apparent increase in T_1 in the fit as we verified by additional tests. Our model also neglects relaxation mediated by phonons, which is justified by the relatively high tunneling currents and the thin MgO support (*28*).

We determine the uncertainties in the fit parameters related to Eq. 2 by standard error analysis. For the fit parameters related to Eq. 1, this approach is hampered by the complexity of the fit procedure. Therefore, we first determine the average experimental noise to signal ratio to be 2%. In the next step, we vary each fit parameter related to Eq. 1 separately until the root mean square deviation of the fit from the experimental spectra grows by 2%. For the Rabi rates, we vary all 119 values at once by an absolute value until the latter 2% deviation is observed.

Additional datasets

Our conclusions are consistent with several additional datasets acquired for a similar range of parameters that we show in fig. S9.

Multiplet calculations

The Fe wave functions, corresponding properties, and matrix elements are obtained from charge transfer multiplet calculations. The

crystal field and charge transfer parameters are taken from previous calculations for the simulation of x-ray absorption spectra of the same system (*27*). In this model, the Fe adatom is described by a combination of d^6 and d^7 configurations coupled by a charge transfer term, in which an electron from a filled substrate oxygen-derived shell is allowed to hop onto the d-shell of Fe via the d_z^2 orbital. The Slater-Condon integrals are rescaled to 75% of their Hartree-Fock value, and the one-electron spin-orbit coupling constant of Fe is taken to be 52 meV for the d^6 and 45 meV for the d^7 configuration. The charge transfer energy between the d^6 and d^7 configurations amounts to 0.5 eV where the hopping parameter to the d_z^2 orbital is 0.85 eV. The crystal field is chosen to be the same for the d^6 and d^7 configurations and is given by $10D_q = -0.13$ eV, $D_s = -0.44$ eV, and $D_t = -0.015$ eV.

DFT calculations

For our first-principles calculations, we use the DFT formalism as implemented in the Vienna ab initio simulation package (VASP) (*35*). For the Fe adatom, we use a 49-atom unit cell with Fe located above a surface oxygen. For the TiH adatoms, we use a 50-atom unit cell with TiH located above a surface oxygen-oxygen bridge. We top both unit cells by 16 Å of vacuum to achieve convergence of forces, and we fix the in-plane lattice constant of the bottom MgO layer to that of Ag(100) (289 pm). Because MgO was shown to act as an efficient filter for the phonon modes of a substrate (*36*), we do not take the Ag substrate into account in this calculation. We use the default VASP projector augmented wave pseudo-potentials and converge the Hellmann-Feynman forces to 10^{-5} eV/Å using a plane-wave energy cutoff of 750 eV and a $3 \times 3 \times 1$ k-point mesh to sample the Brillouin zone. For the exchange-correlation functional, we choose the Perdew-Burke-Ernzerhof revised for solids (PBEsol) form of the generalized gradient approximation (*37*). Our fully relaxed structure with a MgO in-plane lattice constant of 291 pm fits reasonably well to the experimental values of (*36*). The Fe adatom is elevated 194 pm above the protruded surface oxygen. The Ti in the TiH system adatom is elevated 198 pm above the surface oxygen-oxygen bridge, and the bond length of the TiH molecule is 177 pm. An illustration of the unit cells is shown in fig. S7 (A and B).

We calculate the vibrational frequencies and eigenvectors using the frozen-phonon method as implemented in the phonopy package (*38*). The calculations reveal low-frequency localized vibrational modes at the Brillouin zone center involving mainly the motion of the Fe adatom parallel to the surface around 1.9 THz and perpendicular to the surface around 2.9 THz. We obtain the main contributions of the TiH molecule to the vibrational spectrum between 2 and 4 THz and one intramolecular vibrational mode around 10 THz. These modes show up in the vibrational density of states as peaks in the low-frequency regime, as shown in fig. S7 (C and D). Vibrational modes involving mainly the ions of the MgO slab lie at higher frequencies above roughly 5 THz.

We further calculate the Born effective charges using density functional perturbation theory (*39*). In absence of any external electric field, the diagonal component normal to the MgO surface is +0.32 *e* for Fe, +0.61 *e* for Ti, and −0.43 *e* for H, where *e* is the elementary charge.

Next, we model the structural changes of the systems in an applied electric field. The rf electric field used in the experiment has such a low frequency that we expect no excitation of phonons to occur. Instead, we expect the atoms to follow the electric field adiabatically. We therefore apply electric fields with different magnitudes between −1 and 1 V/nm normal to the MgO surface and relax the atomic positions to estimate the induced relative shifts of the Fe and TiH adatoms. The results are shown in Fig. 6 (A and B) and in fig. S7 (E and F).

SUPPLEMENTARY MATERIALS

Supplementary material for this article is available at http://advances.sciencemag.org/cgi/content/full/6/40/eabc5511/DC1

REFERENCES AND NOTES

1. S. Baumann, W. Paul, T. Choi, C. P. Lutz, A. Ardavan, A. J. Heinrich, Electron paramagnetic resonance of individual atoms on a surface. *Science* **350**, 417–420 (2015).
2. K. Yang, Y. Bae, W. Paul, F. D. Natterer, P. Willke, J. L. Lado, A. Ferron, T. Choi, J. Fernandez-Rossier, A. J. Heinrich, C. P. Lutz, Engineering the eigenstates of coupled spin-1/2 atoms on a surface. *Phys. Rev. Lett.* **119**, 227206 (2017).
3. K. Yang, P. Willke, Y. Bae, A. Ferron, J. L. Lado, A. Ardavan, J. Fernandez-Rossier, A. J. Heinrich, C. P. Lutz, Electrically controlled nuclear polarization of individual atoms. *Nat. Nanotechnol.* **13**, 1120–1125 (2018).
4. Y. Bae, K. Yang, P. Willke, T. Choi, A. J. Heinrich, C. P. Lutz, Enhanced quantum coherence in exchange coupled spins via singlet-triplet transitions. *Sci. Adv.* **4**, eaau4159 (2018).
5. P. Willke, W. Paul, F. D. Natterer, K. Yang, Y. Bae, T. Choi, J. Fernandez-Rossier, A. J. Heinrich, C. P. Lutz, Probing quantum coherence in single-atom electron spin resonance. *Sci. Adv.* **4**, eaaq1543 (2018).
6. P. Willke, K. Yang, Y. Bae, A. J. Heinrich, C. P. Lutz, Magnetic resonance imaging of single atoms on a surface. *Nat. Phys.* **15**, 1005–1010 (2019).
7. K. Yang, W. Paul, F. D. Natterer, J. L. Lado, Y. Bae, P. Willke, T. Choi, A. Ferron, J. Fernandez-Rossier, A. J. Heinrich, C. P. Lutz, Tuning the exchange bias on a single atom from 1 mT to 10 T. *Phys. Rev. Lett.* **122**, 227203 (2019).
8. P. Willke, A. Singha, X. Zhang, T. Esat, C. P. Lutz, A. J. Heinrich, T. Choi, Tuning single-atom electron spin resonance in a vector magnetic field. *Nano Lett.* **19**, 8201–8206 (2019).
9. F. D. Natterer, F. Patthey, T. Bilgeri, P. R. Forrester, N. Weiss, H. Brune, Upgrade of a low-temperature scanning tunneling microscope for electron-spin resonance. *Rev. Sci. Instrum.* **90**, 013706 (2019).
10. T. Seifert, S. Kovarik, C. Nistor, L. Persichetti, S. Stepanow, P. Gambardella, Single-atom electron paramagnetic resonance in a scanning tunneling microscope driven by a radio-frequency antenna at 4 K. *Phys. Rev. Res.* **2**, 013032 (2020).
11. P. Willke, Y. Bae, K. Yang, J. L. Lado, A. Ferron, T. Choi, A. Ardavan, J. Fernandez-Rossier, A. J. Heinrich, C. P. Lutz, Hyperfine interaction of individual atoms on a surface. *Science* **362**, 336–339 (2018).
12. K. Yang, W. Paul, S.-H. Phark, P. Willke, Y. Bae, T. Choi, T. Esat, A. Ardavan, A. J. Heinrich, C. P. Lutz, Coherent spin manipulation of individual atoms on a surface. *Science* **366**, 509–512 (2019).
13. T. F. Watson, B. Weber, Y.-L. Hsueh, L. C. Hollenberg, R. Rahman, M. Y. Simmons, Atomically engineered electron spin lifetimes of 30 s in silicon. *Sci. Adv.* **3**, e1602811 (2017).
14. D. Gatteschi, A. L. Barra, A. Caneschi, A. Cornia, R. Sessoli, L. Sorace, EPR of molecular nanomagnets. *Coord. Chem. Rev.* **250**, 1514–1529 (2006).
15. M. Atzori, L. Tesi, E. Morra, M. Chiesa, L. Sorace, R. Sessoli, Room-temperature quantum coherence and rabi oscillations in vanadyl phthalocyanine: Toward multifunctional molecular spin qubits. *J. Am. Chem. Soc.* **138**, 2154–2157 (2016).
16. M. Sterrer, E. Fischbach, T. Risse, H.-J. Freund, Geometric characterization of a singly charged oxygen vacancy on a single-crystalline MgO (001) film by electron paramagnetic resonance spectroscopy. *Phys. Rev. Lett.* **94**, 186101 (2005).
17. T. Risse, D. Hollmann, A. Brückner, In situ electron paramagnetic resonance (EPR)–A unique tool for analysing structure and reaction behaviour of paramagnetic sites in model and real catalysts, in *Catalysis* (The Royal Society of Chemistry, 2015) vol. 27, pp. 1–32.
18. Y. Manassen, R. J. Hamers, J. E. Demuth, A. Castellano Jr., Direct observation of the precession of individual paramagnetic spins on oxidized silicon surfaces. *Phys. Rev. Lett.* **62**, 2531–2534 (1989).
19. A. V. Balatsky, M. Nishijima, Y. Manassen, Electron spin resonance-scanning tunneling microscopy. *Adv. Phys.* **61**, 117–152 (2012).
20. P. Berggren, J. Fransson, Electron paramagnetic resonance of single magnetic moment on a surface. *Sci. Rep.* **6**, 25584 (2016).
21. F. I. Dalidchik, E. Balashov, S. Kovalevskiy, Nature of tunneling electron spin resonance of an isolated surface spin. *JETP Lett.* **105**, 314–318 (2017).
22. J. L. Lado, A. Ferrón, J. Fernández-Rossier, Exchange mechanism for electron paramagnetic resonance of individual adatoms. *Phys. Rev. B* **96**, 205420 (2017).
23. J. R. Gálvez, C. Wolf, F. Delgado, N. Lorente, Cotunneling mechanism for all-electrical electron spin resonance of single adsorbed atoms. *Phys. Rev. B* **100**, 035411 (2019).

24. A. M. Shakirov, A. N. Rubtsov, P. Ribeiro, Spin transfer torque induced paramagnetic resonance. *Phys. Rev. B* **99**, 054434 (2019).
25. A. Ferrón, S. A. Rodríguez, S. S. Gómez, J. L. Lado, J. Fernández-Rossier, Single spin resonance driven by electric modulation of the g-factor anisotropy. *Phys. Rev. Res.* **1**, 033185 (2019).
26. G. Shavit, B. Horovitz, M. Goldstein, Generalized open quantum system approach for the electron paramagnetic resonance of magnetic atoms. *Phys. Rev. B* **99**, 195433 (2019).
27. S. Baumann, F. Donati, S. Stepanow, S. Rusponi, W. Paul, S. Gangopadhyay, I. G. Rau, G. E. Pacchioni, L. Gragnaniello, M. Pivetta, J. Dreiser, C. Piamonteze, C. P. Lutz, R. M. Macfarlane, B. A. Jones, P. Gambardella, A. J. Heinrich, H. Brune, Origin of perpendicular magnetic anisotropy and large orbital moment in Fe atoms on MgO. *Phys. Rev. Lett.* **115**, 237202 (2015).
28. W. Paul, K. Yang, S. Baumann, N. Romming, T. Choi, C. P. Lutz, A. J. Heinrich, Control of the millisecond spin lifetime of an electrically probed atom. *Nat. Phys.* **13**, 403–407 (2017).
29. A. Abragam, B. Bleaney, Electron paramagnetic resonance of transition ions (Clarendon Press, Oxford, 1970).
30. N. Hauptmann, J. W. Gerritsen, D. Wegner, A. A. Khajetoorians, Sensing noncollinear magnetism at the atomic scale combining magnetic exchange and spin-polarized imaging. *Nano Lett.* **17**, 5660–5665 (2017).
31. S. Yan, D.-J. Choi, J. A. Burgess, S. Rolf-Pissarczyk, S. Loth, Control of quantum magnets by atomic exchange bias. *Nat. Nanotechnol.* **10**, 40–45 (2015).
32. N. Krane, C. Lotze, N. Bogdanoff, G. Reecht, L. Zhang, A. L. Briseno, K. J. Franke, Mapping the perturbation potential of metallic and dipolar tips in tunneling spectroscopy on MoS 2. *Phys. Rev. B* **100**, 035410 (2019).
33. J. C. Slonczewski, Conductance and exchange coupling of two ferromagnets separated by a tunneling barrier. *Phys. Rev. B* **39**, 6995–7002 (1989).
34. R. Wiesendanger, Spin mapping at the nanoscale and atomic scale. *Rev. Mod. Phys.* **81**, 1495–1550 (2009).
35. G. Kresse, J. Furthmüller, Self-interaction correction to density functional approximation for many electron systems. *Phys. Rev. B* **54**, 11169–11186 (1996).
36. F. Donati, S. Rusponi, S. Stepanow, C. Wäckerlin, A. Singha, L. Persichetti, R. Baltic, K. Diller, F. Patthey, E. Fernandes, J. Dreiser, Ž. Šljivančanin, K. Kummer, C. Nistor, P. Gambardella, H. Brune, Magnetic remanence in single atoms. *Science* **352**, 318–321 (2016).
37. J. P. Perdew, A. Ruzsinszky, G. I. Csonka, O. A. Vydrov, G. E. Scuseria, L. A. Constantin, X. Zhou, K. Burke, Restoring the density-gradient expansion for exchange in solids and surfaces. *Phys. Rev. Lett.* **100**, 136406 (2008).
38. A. Togo, I. Tanaka, First principles phonon calculations in materials science. *Scr. Mater.* **108**, 1–5 (2015).
39. X. Gonze, C. Lee, Dynamical matrices, Born effective charges, dielectric permittivity tensors, and interatomic force constants from density-functional perturbation theory. *Phys. Rev. B* **55**, 10355–10368 (1997).
40. T. Balashov, T. Schuh, A. Takács, A. Ernst, S. Ostanin, J. Henk, I. Mertig, P. Bruno, T. Miyamachi, S. Suga, W. Wulfhekel, Magnetic anisotropy and magnetization dynamics of individual atoms and clusters of Fe and Co on Pt (111). *Phys. Rev. Lett.* **102**, 257203 (2009).
41. F. De Groot, Multiplet effects in x-ray spectroscopy. *Coord. Chem. Rev.* **249**, 31–63 (2005).
42. O. Gunnarsson, K. Schönhammer, Electron spectroscopies for Ce compounds in the impurity model. *Phys. Rev. B* **28**, 4315–4341 (1983).
43. G. Van der Laan, J. Zaanen, G. Sawatzky, R. Karnatak, J.-M. Esteva, Comparison of x-ray absorption with x-ray photoemission of nickel dihalides and NiO. *Phys. Rev. B* **33**, 4253–4263 (1986).
44. R. D. Cowan, *The theory of Atomic Structure and Spectra* (Univeristy of California Press, 1981).

Acknowledgments

Funding: This work was supported by the Swiss National Science Foundation (SNSF), project no. 200021_163225. D.M.J. received support from the SNSF under project ID 184259. DFT calculations were performed at the Swiss National Supercomputing Centre (CSCS) supported by the project ID s624 and p504. **Author contributions:** T.S.S., S.K., P.G., and S.S. conceived the experiment. T.S.S. and S.K. performed the measurements. D.M.J. and N.A.S. performed the DFT calculations. S.S. developed the density matrix formalism for the Bloch equations and performed the multiplet calculations. T.S.S. analyzed the data and wrote the manuscript with assistance from S.K., P.G., and S.S. All authors commented on the manuscript. **Competing interests:** The authors declare that they have no competing interests. **Data and materials availability:** All data needed to evaluate the conclusions in the paper are present in the paper and/or the Supplementary Materials. Additional data related to this paper may be requested from the authors.

Submitted 30 April 2020
Accepted 13 August 2020
Published 30 September 2020
10.1126/sciadv.abc5511

Citation: T. S. Seifert, S. Kovarik, D. M. Juraschek, N. A. Spaldin, P. Gambardella, S. Stepanow, Longitudinal and transverse electron paramagnetic resonance in a scanning tunneling microscope. *Sci. Adv.* **6**, eabc5511 (2020).